Nanobubbles within a Microbubble: Synthesis and Self-Assembly of Hollow Manganese Silicate and Its Metal-Doped Derivatives

Christopher Cheung Yec and Hua Chun Zeng*

NUS Graduate School for Integrative Sciences and Engineering and Department of Chemical and Biomolecular Engineering, Faculty of Engineering, National University of Singapore, 10 Kent Ridge Crescent, Singapore 119260

ABSTRACT We developed a surface-catalyzed dual templating strategy to synthesize and organize hollow spheres of manganese silicate as well as a wide variety of its metal-doped structural derivatives (where metal dopant = Fe, Co, Ni, Cu, Y, La, Ce, Nd, Eu, Gd, Er, and Yb). The size of hollow spheres obtained is in the range of only 7–9 nm. In addition, the resultant nanospheres can also be formed into an even greater hollow sphere, giving rise to a "bubbles within a bubble" assemblage in the submicrometer regime (*e.g.*, ~200 to 270 nm). The hierarchical hollow structures of this type were further tested for catalytic degradation (or decomposition) of organic dyes and used as solid precursors for transformative synthesis of other silicon-based functional hollow materials.

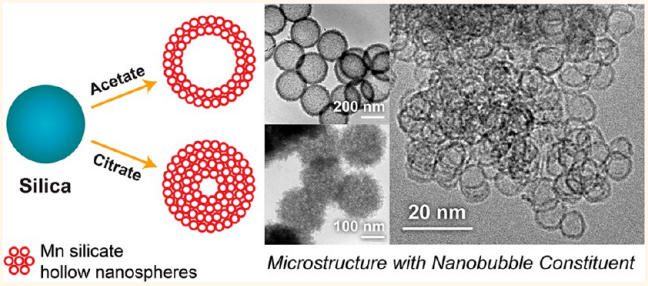

KEYWORDS: hollow materials · manganese silicate · self-assembly · dye degradation · transformative synthesis

Manganese compounds have been commonly regarded as efficient catalysts toward oxidation reaction, and they are widely abundant in nature.[1−3] For instance, the photosystem II protein complex, which is responsible for the photo-oxidation of water in green plants, is composed of a Mn tetramer complex, Mn_4O_4Ca.[4] The manganese compounds not only have a wide range of composition but also have a large variety of morphology. Among these solids, colloidal manganese-based hollow structures stand out as a class of interesting materials, since they may offer improved physicochemical performance owing to significant increase in their surface area to volume ratio.

Colloidal inorganic hollow structures are particles that possess an internal void and have sizes ranging from several angstroms up to several micrometers.[5−7] These hollow structures are usually prepared using template-based methodologies, among which is the use of a gas−liquid interface template.[8] Nevertheless, this method requires forming gas bubbles on which growth units could deposit and thus generate shell morphology. For example, gas bubbles can be introduced to the solution phase through *in situ* reactions that generate gaseous species. Under hydrothermal conditions, very often, organic acids or acid anions decompose into small molecules such as CH_4, CO_2, and H_2, and the gas products depend on an actual reaction pathway.[9−11] For instance, decarboxylation of acetic acid would yield both CH_4 and CO_2, while hydrolysis produces CO_2 and H_2 under such reaction conditions.[10] Furthermore, the decomposition reactions could be hastened through heterogeneous catalysis by the solid wall or any solid phases (such as colloidal particles) available inside a reactor. Therefore, solid phases present in a system can lower the activation energy of reaction[9] and at the same time can determine reaction kinetics of decomposition.[9,10]

Although gas bubble templates have been widely reported for the preparation

* Address correspondence to chezhc@nus.edu.sg.

Received for review April 8, 2014 and accepted May 30, 2014.

Published online May 30, 2014
10.1021/nn501948h

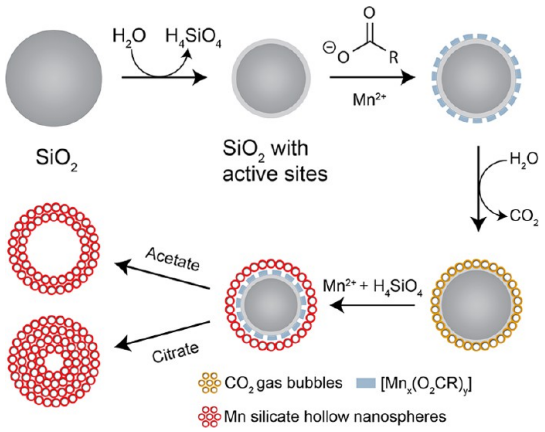

Scheme 1. Schematic illustration of a surface-catalyzed dual templating process, where CO_2 gas bubbles serve as a soft template for deposition of Mn silicate nanospheres (*i.e.*, solid nanobubbles) and a pristine SiO_2 bead serves as a silicon source and works as a hard template for the assemblage of resultant Mn silicate nanospheres.

of micrometer-scale or submicrometer hollow structures, the preparation of hollow structures in a nanoregime (*i.e.*, nanobubbles with a diameter <10 nm) using this approach has not been realized.[8,12−15] Furthermore, self-assembly of resultant nanobubbles into a larger hollow structure appears to be a challenging goal. Herein, we describe a hydrothermal synthesis of nanospheres of manganese silicate and its transition metal- and rare earth metal-doped derivatives as well as self-integration of product nanospheres into submicrometer hollow assemblages. In this synthesis, submicrometer SiO_2 beads serve both as a starting silicon source and as a solid catalyst for the adsorption and decomposition of carboxylate anions. While the *in situ* formed gases serve as a soft template for forming nanobubbles of manganese silicate, the starting silica solid beads function as a hard template for the assembly of these tiny bubbles into an even greater hollow configuration, or a larger "bubble", of manganese silicate. As illustrated in Scheme 1, we will further demonstrate that the decomposition of adsorbed Mn carboxylate complexes on the active surface of SiO_2 beads is the primary mechanism for the formation of a final hierarchical hollow structure. This synthetic strategy can be described as a *surface-catalyzed dual templating process*, since the formation of a nanometer-sized gas template is catalyzed and formed at the surface of the submicrometer solid template. In addition to manganese silicate nanobubbles, metal-doped derivatives of this structure can also be prepared by adding other metal salts in the reaction system. In order to test the applicability of these nanobubbles, we also studied their catalytic property toward the oxidative degradation (or decomposition) of organic dyes and used these nanobubble assemblies as a solid precursor for lithium ion intercalation.

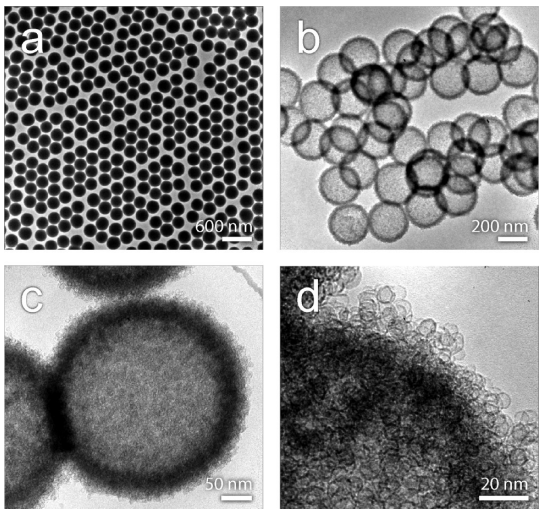

Figure 1. Representative TEM images: (a) SiO_2 precursor beads and (b−d) product samples (*i.e.*, spherically assembled nanobubbles of manganese silicate) synthesized according to Scheme 1 at different magnifications.

RESULTS AND DISCUSSION

Manganese Silicate Nanobubbles. Shown in Figure 1a, spherical SiO_2 beads with a mean diameter of *ca.* 270 nm were first synthesized using a modified Stöber method.[16,17] This solid precursor was mixed with an aqueous solution of manganese acetate and heat-treated under hydrothermal conditions. The process led to the formation of submicrometer hollow spheres in about the same dimensional range, as shown in Figure 1b. Detailed in Figure 1c−d, intriguingly, the hollow spheres were composed of even smaller hollow spheres with diameters only between 7 and 9 nm. We describe this product morphology as *spherically assembled nanobubbles* of manganese silicate, that is, *bubbles within a bubble*.

We believe that *in situ* generation of a gas-bubble template and the related gas−liquid interface are responsible for the formation of this hierarchical hollow structure. As summarized in Scheme 1, first, a small portion of the SiO_2 phase is hydrolyzed to form H_4SiO_4, and at the same time surface active sites are generated for the adsorption of Mn carboxylate species (eq 1).[9] Second, the active sites and associated metal ions (*e.g.*, Mn^{2+}) decrease the activation energy for decomposition of the carboxylate (Scheme 1). Third, the carboxylate groups decompose into CO_2 and other gaseous products under hydrothermal conditions (eqs 2 to 4).[10] Fourth, the tiny gas bubbles form an interface with solution phase that serves as a soft template for the deposition of manganese silicate through ion exchange of Mn^{2+} with H_4SiO_4 (eq 5).[18] Finally, these reactions (eqs 2 to 5) would continue until the SiO_2 phase is totally consumed or dissolved, thus forming submicrometer hollow assemblages comprising nanobubbles of manganese silicate (Scheme 1). In addition, Mn_2SiO_4 can undergo metamorphism to form braunite

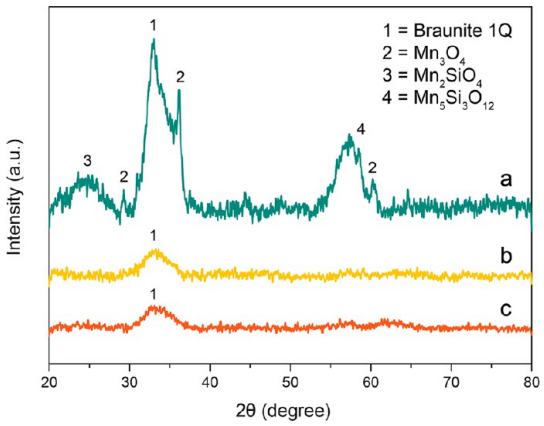

Figure 2. X-ray diffraction patterns of nanobubbles of manganese silicate synthesized with different kinds of carboxylate anions: (a) acetate, (b) maleate, and (c) citrate.

1Q under hydrothermal conditions (eq 6).[18]

$$SiO_{2(s)} + 2H_2O_{(l)} \leftrightarrow H_4SiO_{4(aq)} + \text{active sites} \quad (1)$$

$$CH_3COOH_{(aq)} \rightarrow CH_{4(g)} + CO_{2(g)} \quad (2)$$

$$CH_3COOH_{(aq)} + 2O_{2(g)} \rightarrow 2CO_{2(g)} + 2H_2O_{(l)} \quad (3)$$

$$CH_3COOH_{(aq)} + 2H_2O_{(l)} \rightarrow 2CO_{2(g)} + 4H_{2(g)} \quad (4)$$

$$H_4SiO_{4(aq)} + 2Mn^{2+}{}_{(aq)} \leftrightarrow Mn_2SiO_{4(s)} + 4H^+{}_{(aq)} \quad (5)$$

$$7Mn_2SiO_{4(s)} + 3O_{2(g)} \leftrightarrow 2Mn^{2+}Mn_6{}^{3+}SiO_{12(s)} + 5SiO_{2(s)} \quad (6)$$

Elemental composition of the bubble samples was affirmed with energy dispersive X-ray spectroscopy (SI-1A), and both manganese and silicon were homogeneously distributed. In addition, the atomic ratio between manganese and silica is 1:2.6. In Figure 2a, the X-ray diffraction (XRD) technique indicates the presence of braunite-1Q ($Mn^{2+}Mn_6{}^{3+}SiO_{12}$ or $Mn^{2+}Mn^{3+}{}_6[O_8|SiO_4]$, JCPDS no. 89-5661) and other manganese silicate phases (Mn_2SiO_4, JCPDS no. 74-0716, and $Mn_5Si_3O_{12}$, JCPDS no. 37-0221) with a trace amount of hausmannite (Mn_3O_4, JCPDS no. 80-0382).

The thermal stability of manganese silicate nanobubbles under aerobic conditions was investigated. Surprisingly, the nanobubble morphology was retained even after heating at a temperature as high as 800 °C for 12 h (SI-1B). In fact, heating can be employed as a means to deplete unwanted phases. For instance, the hausmannite phase can be eliminated completely at 700 °C, leaving only pure braunite 1Q (SI-1B) for the nanobubbles. The specific surface area of the as-synthesized nanobubbles was determined to be 316 m^2/g using the Brunauer–Emmett–Teller (BET) method on the N_2 adsorption isotherm (SI-1C). Even after heating at a high temperature of 800 °C for a long period of 12 h, the specific surface area of the sample could still have a value of 52 m^2/g (Table 1). This decrease can be attributed to more densely packed nanobubbles (SI-1C) upon heating. In addition, small micropores were also eliminated in the heating process. Consistently, as shown in Table 1, the pore volume was reduced from 0.151 to 0.068 mL/g, and the pore surface area was decreased from 88.4 to 27.6 m^2/g.

TABLE 1. Summary of BET Analysis and BJH Desorption Analysis for Manganese Silicate Samples

physical property	as-synthesized	thermally treated
surface area	316.1 m^2/g	52.1 m^2/g
pore volume	0.151 mL/g	0.068 mL/g
pore size	3.2 nm	3.0 nm
pore surface area	88.4 m^2/g	27.6 m^2/g

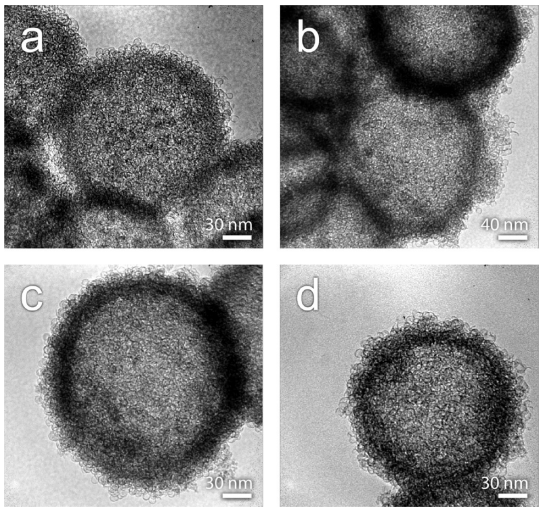

Figure 3. Representative TEM images of spherically assembled nanobubbles of manganese silicate doped with the first-row transition metal elements (a) Fe, (b) Co, (c) Ni, and (d) Cu. The nominal experimental ratio between manganese and dopant was set at 20:1.

On the other hand, these nanobubbles collapsed under long exposure of an electron beam (SI-1D). This change can be described as cavities solidifying into another phase when illuminated by a focused electron beam during transmission electron microscopy (TEM) measurements above the magnification of 150,000× (SI-1D). In addition, we observed that these recrystallized areas possessed an interplanar spacing of 0.21 nm, which corresponds to the {220} crystal planes of hausmannite Mn_3O_4 (SI-1D).

Doped Manganese Silicate Nanobubbles. In addition to the manganese silicate nanobubbles, metal-doped derivatives of this structure were also prepared by mixing other metal salts with manganese acetate during the synthesis. Figures 3 and 4 display some TEM images of the first-row transition metal-doped and rare earth element-doped manganese silicates with a nominal experimental ratio of manganese to dopant of 20:1, respectively. The morphology of doped

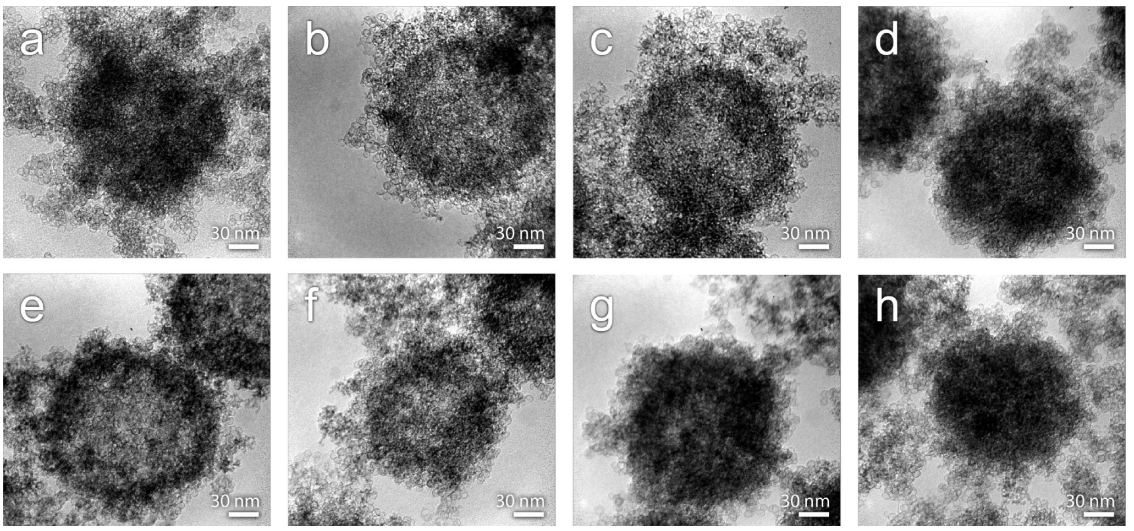

Figure 4. Representative TEM images of spherically assembled nanobubbles of manganese silicate doped with rare earth elements: (a) Y, (b) La, (c) Ce, (d) Nd, (e) Eu, (f) Gd, (g) Er, and (h) Yb. The nominal experimental ratio between manganese and dopant is 20:1.

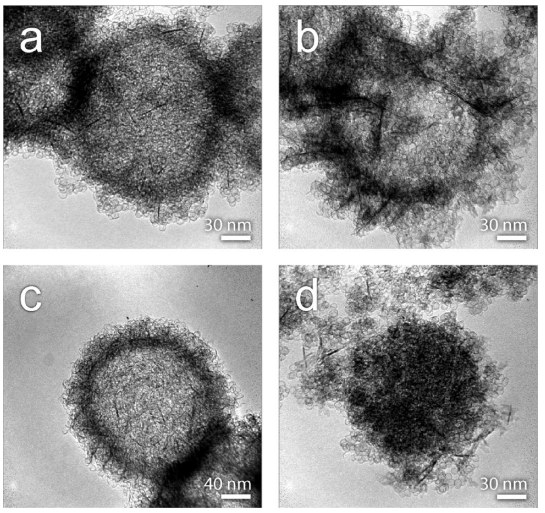

Figure 5. Representative TEM images of manganese silicate doped with other elements: (a) Fe, (b) Co, (c) Ni, and (d) La. The nominal experimental ratio between manganese and dopant is 10:1.

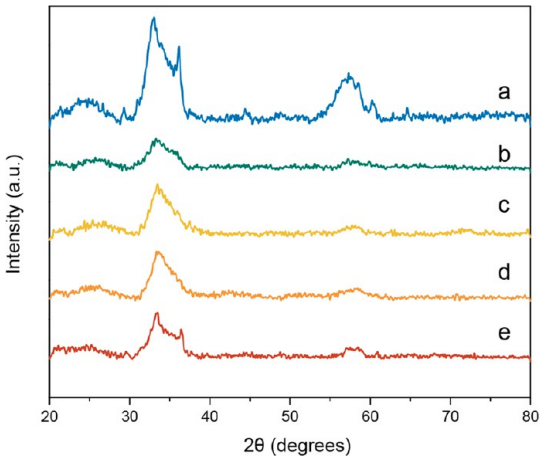

Figure 6. X-ray diffraction patterns of transition metal-doped manganese silicate: (a) undoped, (b) Fe, (c) Co, (d) Ni, and (e) Cu. The nominal experimental manganese to dopant ratio is 20:1.

nanobubbles is similar to that in Figure 1c,d, without noticeable changes.

However, plate-like structures were observed when the experimental ratio of manganese to dopant was decreased to 10:1, as shown in Figure 5. This observation indicates a maximum amount of metal dopant that the final doped nanobubbles can accommodate. When exceeding this threshold limit, heterogeneous growth of a secondary phase would become operative, which will be further discussed in later subsections.

In addition to the TEM characterization, EDX elemental composition analysis and structural mapping of these doped derivatives confirmed the presences of doped elements of Fe, Co, Ni, Cu, Y, La, Ce, Nd, Eu, Gd, Er, and Yb as reported in SI-1A. With the exception of La, this investigation revealed that the actual manganese to dopant ratio was greater than the nominal experimental value (SI-1A). This ratio suggests that the formation of metal-doped manganese silicate nanobubbles might involve ionic exchange or substitution between Mn and the metal dopant during the synthesis. In Figures 6 and 7, X-ray diffraction patterns for both transition metal- and rare earth-doped nanobubbles are very similar to that of the manganese silicate nanobubbles (Figure 2a) except for the case of Ce, which forms a CeO_2 phase.

In addition to the above finding on the similarity, three observations were made in the XRD results. First, the hausmannite Mn_3O_4 peak was observed to be lower than that in the manganese silicate nanobubbles (Figure 2a). Second, with the exception of Ce, no peaks were observed for oxide and silicate variants of the doped metals. Third, the diffraction peak for braunite

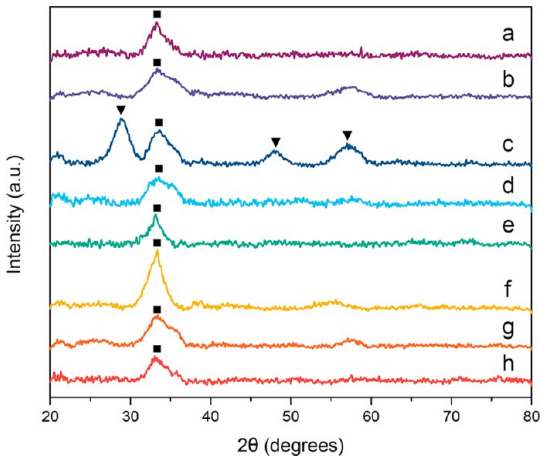

Figure 7. X-ray diffraction patterns of rare earth-doped manganese silicate: (a) Y, (b) La, (c) Ce, (d) Nd, (e) Eu, (f) Gd, (g) Er, and (h) Yb. (■ = braunite 1Q, ▼ = CeO_2). The nominal experimental manganese to dopant ratio is 20:1.

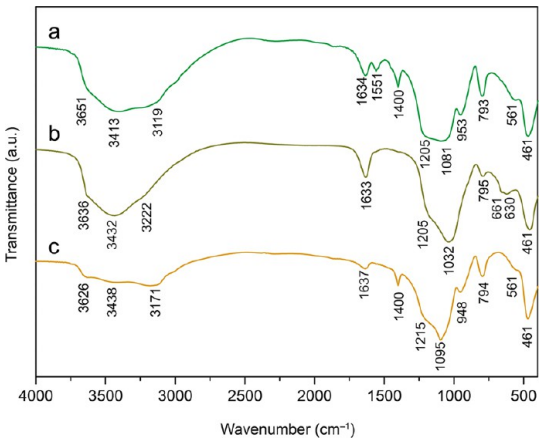

Figure 8. Comparison of FTIR spectra of different samples: (a) sample processed at room temperature for 12 h (SI-2A), (b) nanobubbles of manganese silicate synthesized at 180 °C for 12 h (SI-2A), and (c) SiO_2 precursor beads (Figure 1a).

1Q was observed to shift at higher 2-theta angles for doped manganese silicates. These results may suggest that doping cations do not disrupt the original manganese silicate structure since no additional diffraction peaks for other compounds were observed for most cases. As demonstrated in Figures 3 and 4, a large variety of dopants, both divalent and trivalent metal ions, can be included in the nanobubbles of manganese silicate without altering their structural configuration. Thus, the synthetic approach also allows complex compositional tailoring for product nanobubbles when there is a need (SI-1A).

Synthetic Mechanism of Manganese Silicate Nanobubbles. The formation mechanism of manganese silicate nanobubbles was investigated through several designed experiments. These experiments include determining the pH value of the synthesis system before and after reaction, the presence of RCO_2^- vibration peaks in manganese silicate nanobubbles, the effect of different carboxylate anions and different metal acetates on the final manganese silicate morphology, the effect of manganese and other metal ions on the SiO_2 spheres without carboxylate anions, and, finally, the effect of various synthetic parameters such as temperature, reaction time, pH, and amount of precursor used in the synthesis. On the basis of these experiments, we validated that *in situ* CO_2 evolution occurred during the synthesis. The formation of evolving gas was evidenced by several experimental findings in the following.

The solution pH decreased from 8 to 5 after the hydrothermal process, indicating that CO_2 and H_2CO_3 were formed (eqs 1 to 5). In Figure 8, the IR vibrational spectrum of nanobubbles of manganese silicate did not display RCO_2^- vibrational modes, while those peaks were observed at 1551 and 1400 cm^{-1} for samples processed at room temperature (SI-2A).[19] This result may indicate that acetate anions decompose under hydrothermal conditions. On the other hand, for the starting SiO_2 beads, vibration peaks at 3626, 3438, 3171, 1637, 1215, 1095, 794, and 461 cm^{-1} can be attributed to the presence of water adspecies and silica.[20,21]

In addition to acetate, nanobubbles of manganese silicate can also be produced when other carboxylate anions were used, confirming the indispensability of these anions in synthesis, as shown in Figure 9 (and SI-2B). In Figure 2b,c, XRD patterns for the samples synthesized with manganese maleate and citrate revealed that only pure braunite 1Q phase was formed in these two samples compared with that using acetate anions (Figure 2a; hausmannite Mn_3O_4 was included in this sample). The observed changes can be attributed to different chelating abilities of ligands with manganese ions. The stability of coordination bonds for multidentate maleate and citrate on manganese ions is greater than that for monodentate acetate (SI-2C).[22,23] In this regard, due to its lower stability, a small portion of manganese acetate was converted straight to the Mn_3O_4 spinel even before reacting with H_4SiO_4 (and possibly other silicate oligomers that were produced from condensation of H_4SiO_4; eqs 5 and 6). In comparison, the chance of the latter two manganese carboxylates reacting with H_4SiO_4 would be higher because of their slower decomposition rates. In addition to the phase control, the type of carboxylate groups used in synthesis also determines the interior space of the final aggregation of nanobubbles of manganese silicate. Illustrated in Scheme 1, the resultant shell thickness of spherical assemblages of nanobubbles is thinner if one uses acetate, maleate, or tartrate anions (Figure 9a–c). On the other hand, the central space can be wiped off when citrate anions are used in the synthesis. This significant difference in bubble assemblage can be attributed to the tridentate capacity of citrate. For example, the multiple chelating ability of the citrate ligand not only forms

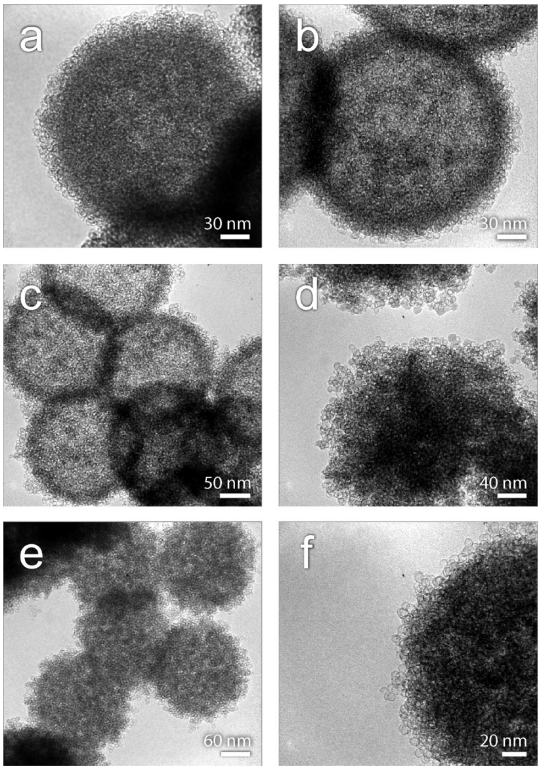

Figure 9. Spherically assembled nanobubbles of manganese silicate prepared with different carboxylate ions. All reaction solutions were heated under hydrothermal conditions at 180 °C for 12 h with 50 mg of SiO_2 precursor beads, 0.80 mmol of $MnSO_4$, and 1.6 mmol of sodium acetate (a), 1.6 mmol of disodium maleate (b), 1.60 mmol of sodium tartrate (c), 1.6 mmol of sodium citrate (d), and 0.30 mmol of sodium citrate (e, f).

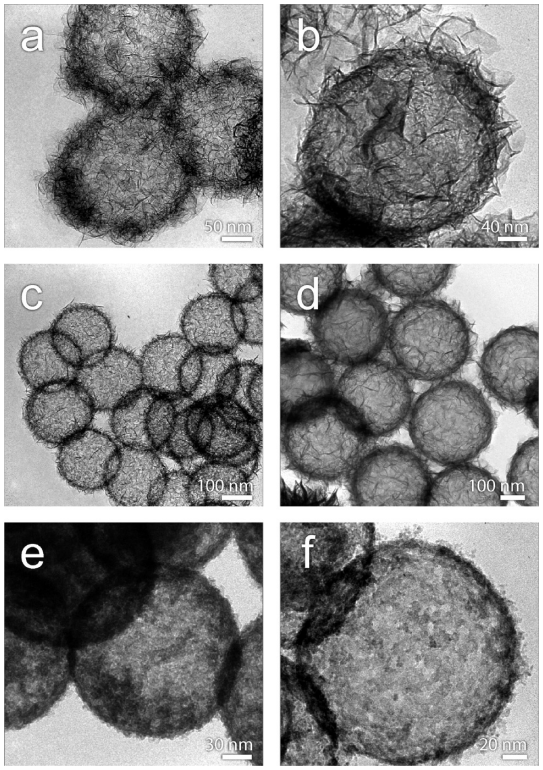

Figure 10. Hollow spheres of metal silicates synthesized using 50 mg of SiO_2 spheres, 5 mmol of $NaCH_3COO$, and 20 mL of H_2O under hydrothermal conditions (180 °C) with (a) 0.80 mmol of $FeSO_4$, (b) 0.10 mmol of $CoSO_4$, (c) 0.20 mmol of $NiSO_4$, (d) 0.125 mmol of $Mn(CH_3COO)_2$ and 0.125 mmol of $Ni(CH_3COO)_2$ (without using $NaCH_3COO$ in this case), (e) 0.80 mmol of $La(NO_3)_3$, and (f) 0.2 mmol of $Ce(CH_3COO)_3$.

manganese-citrate complexes but also brings these complexes onto the surface of silica beads. This extra binding of the citrate anion may provide a capping effect on silica, which prevents the silica core from rapid dissolution (Scheme 1). Thus, more nanobubbles of manganese silicate are formed inwardly and less central interior is left for the assemblages using the Mn citrate precursor (Figure 9d–f). Identical to those in Figure 1, in all these cases, nanobubbles of manganese silicate can also be obtained at a 100% morphological yield. An analysis for the size variation between initial silica and products also supports the above postulation (SI-2B).

When the nominal experimental manganese to dopant ratio was 10:1, other product morphologies were observed (Figure 5) in addition to the nanobubbles. In fact, when this ratio was continuously decreased, the product morphology could be entirely different. Using Stöber silica beads and other transition metal salts, our further syntheses yielded hollow spheres for other transition metal or rare earth metal silicates under similar reaction conditions. Instead of the nanobubbles, however, the shells of the resultant hollow spheres were composed of nanometer-sized thin platelets for the syntheses with transition metal elements Fe, Co, and Ni, while polycrystalline hollow spheres were observed for the cases with rare earth elements La and Ce, as reported in Figure 10. Not unexpectedly, these results are consistent with previous reports on the hollow metal silicate structures (SI-2D).[24−26] In addition to this experiment, we have studied the effect of excluding the carboxylate anion in the synthesis by using metal sulfate precursors. As shown in Figure 11, both $CoSO_4$ and $NiSO_4$ yielded flexible platelets, while $MnSO_4$ formed nanoparticles on the surface of SiO_2- and $FeSO_4$-produced nanocrystals. On the basis of these results, we believe that only Mn^{2+} has a catalytic activity toward the decomposition of carboxylate anions, because the same structures were obtained for Co and Ni silicates with or without carboxylate anions (see Figures 9 and 10). In this regard, the formation of plate-like structures for both Co and Ni silicates can be ascribed simply to the template effect of SiO_2 spheres. The unique catalytic activity of Mn^{2+} may be attributed to two factors, namely, strength of the carboxylate-to-metal coordination bond and possible formation of manganese oxide during the reaction process. As described by Irving and Williams, the stability of high-spin complexes of the first-row transition metals follows this

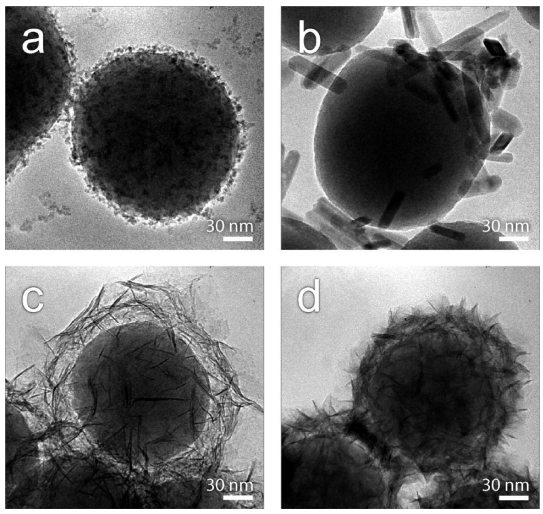

Figure 11. Hydrothermal treatment of SiO_2 with different metal sulfate salts: (a) $MnSO_4$, (b) $FeSO_4$, (c) $CoSO_4$, and (d) $NiSO_4$. Experimental conditions: 0.8 mmol of metal sulfate mixed with 50 mg of SiO_2 beads in 20 mL of H_2O, then heated at 180 °C for 12 h.

series: $Mn^{2+} < Fe^{2+} < Co^{2+} < Ni^{2+} < Cu^{2+} > Zn^{2+}$.[27] Since divalent manganese is the least stable in this series, the decomposition of Mn acetate or with other carboxylate groups to nanostructured gas (CO_2) bubbles is relatively easy. On the other hand, Fe, Co, and Ni complexes share similar stability constants (SI-2C) that result in the formation of similar hollow structures (Figure 10a–c) in the presence of carboxylate anions. This explanation is supported by the presence of carboxylate RCO_2^- vibration modes (1547–1558 and 1410–1428 cm^{-1}; SI-2D)[19] on the hollow spheres of Fe, Co, and Ni silicates because of slower decomposition reactions.

In addition, literature data on the thermal decomposition of acetate salts of Mn, Co, Ni, and Cu follow a similar trend, which also extends to malonate salts.[28–33] On the other hand, adsorbed carboxylate groups were also found in La and Ce silicates (Figure 10e,f). For this reason, easy decomposition of Mn carboxylate implicates the readiness of the aggregative gas template and thus deposition of the nanobubbles of manganese silicate. Although the proposed synthetic mechanism is supported by our experiments, it should be pointed out that direct observation of *in situ* formation of the manganese silicate nanobubbles is difficult to make at this stage of research because of the required hydrothermal conditions.

As mentioned earlier, the catalytic activity of Mn^{2+} toward carboxylate decomposition may also be attributed to the formation of manganese oxides under the hydrothermal conditions. Manganese oxides of different valence have been reported to function as an effective catalyst toward oxidation reaction. Therefore, the formation of CO_2 gas bubbles from carboxylate oxidation is possible.[34–37] In our present study, the formation of manganese oxides was also confirmed by hydrothermal treatment of the $Mn(CH_3COO)_2$ salt in the absence of SiO_2 spheres (SI-2E). These polydispersed crystallites were determined to be a mixture of MnO, Mn_3O_4, MnO(OH), $Mn_{2.03}O_4$, and MnO_2 and other manganese oxide phases through XRD (SI-2E). This experiment confirms that manganese oxides can be formed under hydrothermal conditions, and therefore the resultant manganese oxides can also catalyze the oxidation of carboxylate anions.

Apart from the reaction temperature (SI-2A), other synthetic parameters such as reaction temperature, pressure, time, pH value, and precursor type and amount have also been investigated and optimized (SI-2F to SI-2J). In general, high reaction temperature and long reaction time favor the formation of nanobubbles, and a hydrothermal condition is essential since it may prevent the *in situ* formed gas bubbles from escaping to the gas phase. We also found that an acidic starting solution (pH < 4.8) does not favor nanobubbles on the surface of silica owing to the difficulty of forming carboxylate anions and therefore the resultant Mn carboxylate complexes. Furthermore, nanobubbles of manganese silicate were also obtained from the reaction with $MnSO_4$ and Na_2CO_3, while only hollow microspheres were synthesized from the reaction using $MnSO_4$ and Na_2HPO_4 under alkaline conditions (SI-2J). These results support the observation that gas-forming species are required to generate nanobubbles. All the observations are consistent with the synthetic path proposed in Scheme 1.

Although CO_2 gas bubbles formed at the surface SiO_2 template are both thermodynamically and kinetically dynamic, other chemical constituents (*e.g.*, Mn^{2+}, RCO_2^-) are also present in solution. These solution species would accumulate and solidify on the gas/liquid interface of the CO_2 gas bubble, thus lowering its surface tension and preventing its detachment from the SiO_2 substrate.[38,39] In addition to this explanation, we also observed that the surface of partially hydrolyzed SiO_2 spheres is rather rough, exhibiting surface grooves of various sizes. Thus, the rough SiO_2 substrate may also help to entrap CO_2 gas bubbles formed during carboxylate decomposition.

Catalytic Applications of Manganese Silicate Nanobubbles. Due to the excellent catalytic activity of manganese-based solid compounds and the unique morphology of these hollow structures, we chose to study their adsorption and catalytic properties toward the degradation of cationic organic dyes, *e.g.*, rhodamine-6G and methylene blue, *via* an advanced oxidation process (AOP).[40,41] In this study, reported in Figure 12 (also SI-3A), the nanobubbles of manganese silicate and the dye solution were allowed to establish an adsorption equilibrium for a period of 60 min. After establishing equilibrium, 20% and 30% of the initial rhodamine 6G and methylene blue molecules were adsorbed on the

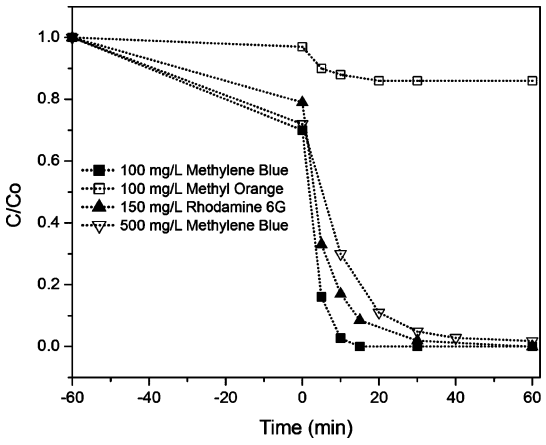

Figure 12. Relative concentration (C/C_0) profiles of methylene blue, rhodamine 6G, and methyl orange during adsorption (−60 to 0 min) and catalytic decomposition (0 to 60 min) processes at 60 °C. A 20 mg amount of nanobubbles of manganese silicate and 100 mL of a dye solution were used in each experiment. C is process concentration and C_0 is starting concentration; the oxidant H_2O_2 was added at 0 min.

nanobubbles of manganese silicate, respectively. Upon the addition of oxidant H_2O_2, the concentration of methylene blue (100 mg/L) decreased to *ca.* 18% of its initial value after 5 min, and the reaction finished just in a total of 15 min (Figure 12). Similarly, the concentration of rhodamine 6G decreased to 18% of its initial value after 10 min, and the reaction finished within 30 min (Figure 12). Our further experiments showed that the manganese silicate nanobubbles can catalyze the degradation of methylene blue at an even higher concentration (500 mg/L). In contrast to methylene blue and rhodamine 6G, which are cationic dyes, both adsorption and catalytic activity of these manganese silicate nanobubbles toward degradation and/or decomposition of anionic dyes were poor. As an example of this type of organic dyes, in Figure 12, we also showed the adsorption−degradation process of methyl orange (an anionic organic dye). These results revealed that the surface charge of the manganese silicate nanobubbles is negative, as evidenced by the presence of Si-OH species (Figure 8). In this regard, the nanobubbles of manganese silicate can also be used to perform selective treatment of organic dyes, since they can preferably adsorb and catalyze the degradation of cationic organic dyes.

In order to exploit other applications, we also investigated the exchangeability of metal ions for the prepared hollow structures. When the self-assembled nanobubbles of manganese silicate were used as a template for lithium intercalation, polycrystalline hollow spheres of Li_2SiO_3 and $LiMn_2O_4$ were observed (SI-3B). In view of their tailorable composition and unique morphology, such hollow structures may find their applications as cathode materials for secondary Li-ion batteries.[42−44] Therefore, the nanobubbles of manganese silicate (Figures 1 and 9) and their metal-doped derivatives (Figures 3 and 4), including other spherical hollow structures of transition metal silicates synthesized in this work (Figure 10), can be used as solid precursors for the preparation of other functional materials.

In addition to this application, Gd-doped manganese silicate nanobubbles are magnetically responsive since its aqueous suspension can be separated by exposing it in a magnetic field (SI-3C). This result is consistent with our previous work, wherein Gd-based colloidal coordination polymer spheres exhibited magnetic property.[45]

CONCLUSIONS

In summary, hierarchical hollow assemblages (∼200 to 270 nm) composed of smaller nanobubbles (<10 nm) of manganese silicate and their metal-doped derivatives can be prepared under hydrothermal conditions using a surface-catalyzed dual templating approach. In this process, adsorption and decomposition of Mn carboxylates are important in gas bubble generation since these processes dictate the product morphology. In addition, Mn^{2+} also serves as a catalyst toward the decomposition of carboxylate anions, while a strong metal to silica interaction was observed for other transition metals, which can be described as a templating effect. The nanobubbles of manganese silicate obtained can work as an effective heterogeneous catalyst and serve as a versatile solid precursor for transformative synthesis of other functional hollow materials.

EXPERIMENTAL SECTION

Chemicals and Reagents. The following chemicals were used in this work: tetraethyl orthosilicate (TEOS, ≥99.0%, Aldrich), ammonia solution (25%, Merck), manganese(II) acetate tetrahydrate ($Mn(CH_3COO)_2\cdot 4H_2O$, ≥99%, Aldrich), manganese(II) sulfate monohydrate (99%, Alfa Aesar), sodium acetate anhydrous (99%, Alfa Aesar), maleic acid disodium salt anhydrous (≥98.0%, Fluka), sodium tartrate dihydrate dibasic (≥98.0%, Riedel-de Haen), sodium citrate tribasic dihydrate (≥99.0%, Sigma-Aldrich), iron(II) sulfate heptahydrate (≥99.0%, Sigma-Aldrich), cobalt(II) sulfate heptahydrate (≥99%, Sigma-Aldrich), nickel(II) sulfate hexahydrate (99%, Sigma), copper(II) sulfate pentahydrate (99.5%, Nacalai Tesque), yttrium(III) nitrate hexahydrate (99.9%, Strem Chemicals), lanthanum(III) nitrate hexahydrate (≥96.0%, Merck), cerium(III) nitrate hexahydrate (99%, Aldrich), neodymium(III) nitrate hexahydrate (99.9%, Strem Chemicals), europium(III) nitrate hexahydrate (99.9%, Alfa Aesar), gadolinium(III) nitrate hexahydrate (99.9%, Strem Chemicals), erbium(III) nitrate hydrate (99.9%, Strem Chemicals), ytterbium(III) nitrate hydrate (99.9%, Alfa Aesar), methylene blue (C.I. 62015, Merck), rhodamine 6G (95%, Sigma), methyl orange (C.I. 13025, Merck), hydrogen peroxide solution (30%, Merck), and deionized water.

Synthesis of SiO_2 Precursor Beads. SiO_2 beads were synthesized according to a previous report with minor modifications.[16] Briefly, TEOS (2.5 mL) was mixed with ethanol (46.0 mL) under

magnetic stirring (1000 rpm). Ammonia solution (5 mL) was added into the solution and was stirred for 4 h. Afterward, the solution was centrifuged at 3000*g* for 10 min, and the resulting precipitate (silica beads) was washed with ethanol (30 mL) and dried in an electric oven at 60 °C for 30 min.

Synthesis of Manganese Silicate Nanobubbles. In a typical synthesis, 0.80 mmol of $Mn(CH_3COO)_2 \cdot 4H_2O$ was dissolved in 10 mL of deionized water in a Teflon liner, while the above prepared SiO_2 beads (50 mg) were dispersed in another 10 mL of deionized water with ultrasonication. Afterward, the SiO_2 suspension was poured into the $Mn(CH_3COO)_2$ in the Teflon liner and was stirred for 5 min. The Teflon liner was then transferred to a stainless steel autoclave and was heated at 180 °C for 12 h inside an electric oven. The autoclave was cooled at room temperature for 3 h. The product solution was centrifuged at 4000*g* for 2 min, and the resulting precipitate was washed with deionized water (10 mL), followed by ethanol (10 mL), and the precipitate was dried at 80 °C for 6 h.

Synthesis of Doped Manganese Silica Nanobubbles. The synthetic procedure for metal-doped nanobubbles of manganese silica was similar to that used in nanobubbles of manganese silicate with a slight modification. Briefly, 0.04 mmol of transition metal salts such as $FeSO_4$, $CoSO_4$, $NiSO_4$, or $CuSO_4$ or rare earth metal salts such as $Y(NO_3)_3$, $La(NO_3)_3$, $Ce(NO_3)_3$, $Nd(NO_3)_3$, $Eu(NO_3)_3$, $Gd(NO_3)_3$, $Er(NO_3)_3$, or $Yb(NO_3)_3$ and 0.80 mmol of $Mn(CH_3COO)_2 \cdot 4H_2O$ were dissolved in 10 mL of H_2O in a Teflon liner to obtain a Mn to dopant ratio of 20:1. During this period, SiO_2 beads (50 mg) were dispersed in another 10 mL of deionized water with ultrasonication. Afterward, the SiO_2 suspension was poured into the $Mn(CH_3COO)_2$ and dopant solution in the Teflon liner and was stirred for 5 min. The Teflon liner was then transferred to a stainless steel autoclave and was heated at 180 °C for 12 h inside an electric oven. The autoclave was cooled at room temperature for 3 h. The product solution was centrifuged at 4000*g* for 2 min, the resultant precipitate was washed with deionized water (10 mL), followed by ethanol (10 mL), and the precipitate was dried at 80 °C for 6 h.

Evaluation of Catalytic Activity. The degradation of organic dye molecules *via* an advanced oxidation process was investigated with the nanobubbles of manganese silicate. This catalyst (20 mg) was dispersed in 100 mL of various dye solutions: methylene blue (100 mg/L), rhodamine 6G (150 mg/L), and methyl orange (100 mg/L). On the other hand, 50 mg of the same nanobubble catalyst was also used for the degradation of a higher concentration of methylene blue (500 mg/L). The prepared solution was immersed in a water bath at 60 °C for 1 h under magnetic stirring. Afterward, hydrogen peroxide (10 mL, 30%) was added into the solution and was stirred for 1 h. During this period, liquid samples (5 mL) were withdrawn from the solution and were centrifuged at 4000*g* for 1 min. The resulting supernatant was diluted 10-fold before transferring into a quartz cuvette (path length, 10 mm), and its absorption spectra were acquired using UV–vis spectroscopy (UV-2450, Shimadzu). Absorption peaks at 665, 526, and 463 nm were used respectively to determine the concentrations of methylene blue, rhodamine 6G, and methyl orange in the supernatant.

Materials Characterization. Morphology and structure of the samples were investigated with transmission electron microscopy (JEM-2010, 200 kV) and high-resolution TEM (JEM-2100F, 200 kV). Chemical bonding information was acquired using Fourier transformed infrared spectroscopy (FTIR, FTS-2500ARX, Bio-Rad). The composition and elemental distribution were determined using energy dispersive X-ray spectroscopy (EDX, Oxford Instruments). Crystallographic information was established by power X-ray diffraction (D8 Advanced, Bruker, Cu Kα radiation at 1.5406 Å). Nitrogen adsorption and desorption isotherms were measured with a gas-sorption analyzer (NOVA-3000, Quantachrome Instruments). The specific surface area of the sample and its pore size distribution were calculated using the Brunauer–Emmett–Teller (BET) method and Barrett–Joyner–Halenda (BJH) desorption curve analysis, respectively.

Conflict of Interest: The authors declare no competing financial interest.

Acknowledgment. C.C.Y. would like to thank NUS Graduate School for Integrative Sciences and Engineering for providing his postgraduate scholarship. The authors would also like to acknowledge NUS and GSK Singapore for financial support of this work.

Supporting Information Available: Additional TEM images, XRD patterns, stability constants of transition metal acetates, FTIR spectra of other transition metal silicates, N_2 adsorption–desorption isotherms for manganese silicates, EDX elemental mappings and spectra, UV–vis spectra during dye decomposition, and lithium ion intercalation results. This material is available free of charge *via* the Internet at http://pubs.acs.org.

REFERENCES AND NOTES

1. Shen, Y. F.; Zerger, R. P.; Deguzman, R. N.; Suib, S. L.; Mccurdy, L.; Potter, D. I.; Oyoung, C. L. Manganese Oxide Octahedral Molecular Sieves: Preparation, Characterization, and Applications. *Science* **1993**, *260*, 511–515.
2. Tusar, N. N.; Jank, S.; Glaser, R. Manganese-Containing Porous Silicates: Synthesis, Structural Properties and Catalytic Applications. *ChemCatChem.* **2011**, *3*, 254–269.
3. Hage, R.; Iburg, J. E.; Kerschner, J.; Koek, J. H.; Lempers, E. L. M.; Martens, R. J.; Racherla, U. S.; Russell, S. W.; Swarthoff, T.; Vavliet, M. R. P.; *et al.* Efficient Manganese Catalysts for Low-Temperature Bleaching. *Nature* **1994**, *369*, 637–639.
4. Yano, J.; Kern, J.; Sauer, K.; Latimer, M. J.; Pushkar, Y.; Biesiadka, J.; Loll, B.; Saenger, W.; Messinger, J.; Zouni, A.; *et al.* Where Water is Oxidized to Dioxygen: Structure of the Photosynthetic Mn_4Ca Cluster. *Science* **2006**, *314*, 821–825.
5. Du, H.; Jiao, L.; Wang, Q.; Yang, J.; Guo, L.; Si, Y.; Wang, Y.; Yuan, H. Facile Carbonaceous Microsphere Templated Synthesis of Co_3O_4 Hollow Spheres and Their Electrochemical Performance in Supercapacitors. *Nano Res.* **2012**, *6*, 87–98.
6. Sun, Z.; Liao, T.; Liu, K.; Jiang, L.; Kim, J. H.; Dou, S. X. Robust Superhydrophobicity of Hierarchical ZnO Hollow Microspheres Fabricated by Two-Step Self-Assembly. *Nano Res.* **2013**, *6*, 726–735.
7. Wang, Z.; Zhou, L.; Lou, X. W. Metal Oxide Hollow Nanostructures for Lithium-Ion Batteries. *Adv. Mater.* **2012**, *24*, 1903–1911.
8. Peng, Q.; Dong, Y.; Li, Y. ZnSe Semiconductor Hollow Microspheres. *Angew. Chem., Int. Ed.* **2003**, *42*, 3027–3030.
9. Palmer, D. A.; Drummond, S. E. Thermal Decarboxylation of Acetate. Part I. The Kinetics and Mechanism of Reaction in Aqueous Solution. *Geochim. Cosmochim. Acta* **1986**, *50*, 813–823.
10. McCollom, T. M.; Seewald, J. S. Experimental Study of the Hydrothermal Reactivity of Organic Acids and Acid Anions: II. Acetic Acid, Acetate, and Valeric Acid. *Geochim. Cosmochim. Acta* **2003**, *67*, 3645–3664.
11. Onwudili, J. A.; Williams, P. T. Hydrothermal Reactions of Sodium Formate and Sodium Acetate as Model Intermediate Products of the Sodium Hydroxide-Promoted Hydrothermal Gasification of Biomass. *Green Chem.* **2010**, *12*, 2214–2224.
12. Gu, F.; Li, C. Z.; Wang, S. F.; Lü, M. K. Solution-Phase Synthesis of Spherical Zinc Sulfide Nanostructures. *Langmuir* **2006**, *22*, 1329–1332.
13. Wu, C. Z.; Xie, Y.; Lei, L. Y.; Hu, S. Q.; OuYang, C. Z. Synthesis of New-Phased VOOH Hollow "Dandelions" and Their Application in Lithium-Ion Batteries. *Adv. Mater.* **2006**, *18*, 1727–1732.
14. Wu, Z. C.; Yu, K.; Zhang, S. D.; Xie, Y. Hematite Hollow Spheres with a Mesoporous Shell: Controlled Synthesis and Applications in Gas Sensor and Lithium Ion Batteries. *J. Phys. Chem. C* **2008**, *112*, 11307–11313.
15. Wan, J.; Stone, H. A. Coated Gas Bubbles for the Continuous Synthesis of Hollow Inorganic Particles. *Langmuir* **2011**, *28*, 37–41.
16. Yao, K. X.; Zeng, H. C. Simultaneous Chemical Modification and Structural Transformation of Stöber Silica Spheres for Integration of Nanocatalysts. *Chem. Mater.* **2012**, *24*, 140–148.
17. Stöber, W.; Fink, A.; Bohn, E. Controlled Growth of Monodisperse Silica Spheres in the Micron Size Range. *J. Colloid Interface Sci.* **1968**, *26*, 62–69.

18. Deer, W. A.; Howie, R. A.; Zussman, J. *Rock-Forming Minerals, Orthosilicates*, 2nd ed., Vol. 1A; The Geological Society, 1982; p 348.
19. Ito, K.; Bernstein, H. J. The Vibrational Spectra of the Formate, Acetate, and Oxalate Ions. *Can. J. Chem.* **1956**, *34*, 170–178.
20. Galeener, F. L.; Lucovsky, G. Longitudinal Optical Vibrations in Glasses: GeO_2 and SiO_2. *Phys. Rev. Lett.* **1976**, *37*, 1474–1478.
21. Wakabayashi, H.; Tomozawa, M. Diffusion of Water into Silica Glass at Low Temperature. *J. Am. Ceram. Soc.* **1989**, *72*, 1850–1855.
22. Schwarzenbach, G. Der Chelateffekt. *Helv. Chim. Acta* **1952**, *35*, 2344–2359.
23. Hancock, R. D.; Martell, A. E. The Chelate, Cryptate and Macrocyclic Effects. *Comments Inorg. Chem.* **1988**, *6*, 237–284.
24. Wang, J.; Xu, C. H.; Yao, M.; Chen, J.; Xu, G. J. A Facile Route to Prepare Hierarchical Magnetic Cobalt−Silica Hollow Nanospheres with Tunable Shell Thickness. *J. Nanopart. Res.* **2009**, *12*, 1161–1166.
25. Fang, Q.; Xuan, S.; Jiang, W.; Gong, X. Yolk-like Micro/Nanoparticles with Superparamagnetic Iron Oxide Cores and Hierarchical Nickel Silicate Shells. *Adv. Funct. Mater.* **2011**, *21*, 1902–1909.
26. Wang, Y.; Tang, C.; Deng, Q.; Liang, C.; Ng, D. H. L.; Kwong, F.; Wang, H.; Cai, W.; Zhang, L.; Wang, G. A Versatile Method for Controlled Synthesis of Porous Hollow Spheres. *Langmuir* **2010**, *26*, 14830–14834.
27. Irving, H.; Williams, R. J. P. The Stability of Transition-Metal Complexes. *J. Chem. Soc.* **1953**, 3192–3210.
28. Mohamed, M. A.; Halawy, S. A. Kinetic and Mechanistic Study of the Non-isothermal Decomposition of Manganese(II) Acetate Tetrahydrate. *Thermochim. Acta* **1994**, *242*, 173–186.
29. Mohamed, M. A.; Halawy, S. A.; Ebrahim, M. M. The Non-isothermal Decomposition of Cobalt Acetate Tetrahydrate. *J. Therm. Anal.* **1994**, *41*, 387–404.
30. Mohamed, M. A.; Halaway, S. A.; Ebrahim, M. M. Non-Isothermal Tetrahydrate Decomposition of Nickel Acetate Tetrahydrate. *J. Anal. Appl. Pyrolysis* **1993**, *27*, 109–118.
31. Mohamed, M. A. Non-isothermal Dehydration and Decomposition of Manganese(II) Malonate Dihydrate. *J. Anal. Appl. Pyrolysis* **1994**, *30*, 59–72.
32. Mohamed, M. A.; Galwey, A. K.; Halawy, S. A. Kinetic and Thermodynamic Study of the Non-isothermal Decompositions of Cobalt Malonate Dihydrate and of Cobalt Hydrogen Malonate Dihydrate. *Thermochim. Acta* **2000**, *346*, 91–103.
33. Mohamed, M. A.; Galwey, A. K.; Halawy, S. A. Kinetic and Thermodynamic Studies of the Non-isothermal Decompositions of Nickel Malonate Dihydrate and Nickel Hydrogen Malonate Dihydrate. *Thermochim. Acta* **1998**, *323*, 27–36.
34. Gandhe, A. R.; Rebello, J. S.; Figueiredo, J. L.; Fernandes, J. B. Manganese Oxide OMS-2 as an Effective Catalyst for Total Oxidation of Ethyl Acetate. *Appl. Catal., B* **2007**, *72*, 129–135.
35. Dharmarathna, S.; King'ondu, C. K.; Pedrick, W.; Pahalagedara, L.; Suib, S. L. Direct Sonochemical Synthesis of Manganese Octahedral Molecular Sieve (OMS-2) Nanomaterials Using Cosolvent Systems, Their Characterization, and Catalytic Applications. *Chem. Mater.* **2012**, *24*, 705–712.
36. Son, Y. C.; Makwana, V. D.; Howell, A. R.; Suib, S. L. Efficient, Catalytic, Aerobic Oxidation of Alcohols with Octahedral Molecular Sieves. *Angew. Chem., Int. Ed.* **2001**, *40*, 4280–4283.
37. Jiao, F.; Frei, H. Nanostructured Manganese Oxide Clusters Supported on Mesoporous Silica as Efficient Oxygen-evolving Catalysts. *Chem. Commun.* **2010**, *46*, 2920–2922.
38. Ducker, W. A. Contact Angle and Stability of Interfacial Nanobubbles. *Langmuir* **2009**, *25*, 8907–8910.
39. Seddon, J. R. T.; Lohse, D.; Ducker, W. A.; Craig, V. S. J. A Deliberation on Nanobubbles at Surfaces and in Bulk. *ChemPhysChem* **2012**, *13*, 2179–2187.
40. Tušar, N. N.; Maučec, D.; Rangus, M.; Arčon, I.; Mazaj, M.; Cotman, M.; Pintar, A.; Kaučič, V. Manganese Functionalized Silicate Nanoparticles as a Fenton-Type Catalyst for Water Purification by Advanced Oxidation Processes (AOP). *Adv. Funct. Mater.* **2012**, *22*, 820–826.
41. Park, J.; Jang, I.; Kwon, B.; Jang, S.; Oh, S. Formation of Manganese Oxide Shells on Silica Spheres with Various Crystal Structures Using Surfactants for the Degradation of Methylene Blue Dye. *Mater. Res. Bull.* **2013**, *48*, 469–475.
42. Lou, X. W.; Archer, L. A.; Yang, Z. C. Hollow Micro-/Nanostructures: Synthesis and Applications. *Adv. Mater.* **2008**, *20*, 3987–4019.
43. Rangappa, D.; Murukanahally, K. D.; Tomai, T.; Unemoto, A.; Honma, I. Ultrathin Nanosheets of Li_2MSiO_4 (M = Fe, Mn) as High-Capacity Li-Ion Battery Electrode. *Nano Lett.* **2012**, *12*, 1146–1151.
44. He, G.; Popov, G.; Nazar, L. F. Hydrothermal Synthesis and Electrochemical Properties of Li_2CoSiO_4/C Nanospheres. *Chem. Mater.* **2013**, *25*, 1024–1031.
45. Li, C. C.; Zeng, H. C. Coordination Chemistry and Antisolvent Strategy to Rare-Earth Solid Solution Colloidal Spheres. *J. Am. Chem. Soc.* **2012**, *134*, 19084–19091.